Robust Control of a Two-Terminal Cryogenic Current Comparator

M. E. Bierzychudek, R. S. Sánchez–Peña, *Senior Member, IEEE*, and Alejandra Tonina

***Abstract*—A digital $H\infty$ controller for a two-terminal cryogenic current comparator is designed. To this end, a set of mathematical models covering the actual system is proposed. Simulation results compare the open- and closed-loop systems based on the proposed controller and the traditional integral control. According to these results, the new controller can significantly reduce the noise in the superconducting quantum interference device sensor.**

***Index Terms*—Current comparators, current measurement, H-infinity control, resistance measurements, superconducting quantum interference device (SQUID).**

I. Introduction

THE cryogenic current comparator (CCC) bridge is widely used in high-accuracy metrology. It is the chosen system for many national metrology institutes (NMIs) to calibrate standard resistors against the quantum Hall resistance. In this system, a superconducting quantum interference device (SQUID) sensor is used to fix the current ratio. A SQUID can detect extremely small changes of magnetic field, and it is a nonlinear device. This combination of characteristics can produce rectification, flux jumps, or saturation of the SQUID controller. These undesired effects can increase the standard deviation, produce systematic errors [1], or even impede the measurement. Since its origin, the SQUID stabilization and a low null error were obtained using an analog integral controller. Recently, more complex control strategies have been applied. For example, some NMIs have included digital filters in the current sources [2] or have used feedforward techniques [3] to decrease the effect of the time constants difference between the arms of a four-terminal CCC. In addition, an NMI has presented a dynamic model of the CCC and a control strategy [4]. In a more recent publication, a high-frequency control loop has been applied to decrease the effect of noise in the SQUID [5]. Aside from these works, little has been published on the dynamic model of the CCC and its control.

Manuscript received June 29, 2012; revised November 2, 2012; accepted November 14, 2012. Date of publication February 20, 2013; date of current version May 8, 2013. The Associate Editor coordinating the review process for this paper was Dr. George Jones.

M. E. Bierzychudek and A. Tonina are with the Quantum Standards Laboratory, Electricity Division, Instituto Nacional de Tecnología Industrial, San Martín B1650KNA, Argentina (e-mail: marcosb@inti.gob.ar; atonina@inti.gob.ar).

R. S. Sánchez–Peña is with the Consejo Nacional de Investigaciones Científícas y Técnicas, Buenos Aires C1033AAJ, Argentina, and also with Buenos Aires Institute of Technology (ITBA), Buenos Aires C1106ACD, Argentina (e-mail: rsanchez@itba.edu.ar).

Color versions of one or more of the figures in this paper are available online at http://ieeexplore.ieee.org.

Digital Object Identifier 10.1109/TIM.2013.2240954

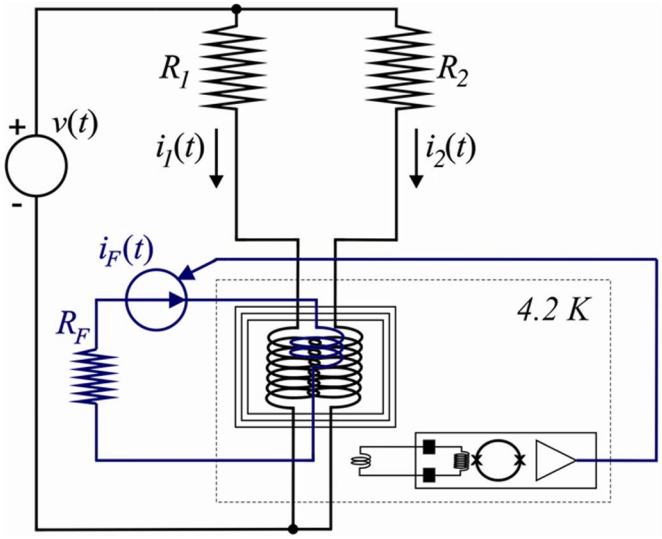

Fig. 1. Diagram of the two-terminal CCC. Note that, if $i_2(t) = 0$, the system will be quite similar to an ultralow current amplified based on a CCC.

Our work presents analysis, synthesis, and simulations that contribute to understanding the CCC dynamic behavior and obtaining a better stabilization. Here, an $H\infty$ controller is applied to a particular case, a two-terminal CCC [6]. The goal of the $H\infty$ control technique is to synthesize a controller that stabilizes and keeps the output of the system below a given threshold for a class of exogenous disturbances and a set of models that represent the physical system. This is achieved minimizing the infinity norm of the transfer function from the disturbance to the output [7], [8]. Robust control theory was developed in the early 1980s and has been applied to many complex systems since then.

II. Two-Terminal CCC Model

The two-terminal CCC has been fully described in [6] and [9]. Each resistor $(R_{1,2})$ to be compared is connected in series with a winding $(N_{1,2})$ forming the two arms of the bridge; see Fig. 1. A direct voltage source $(v(t))$ is connected in parallel. The magnetic fluxes produced by the resistor's currents $(i_{1,2}(t))$ have opposite directions, and the flux difference is measured with a dc SQUID. The bridge is balanced using the SQUID output voltage to drive a feedback current $(i_F(t))$ in a third winding (N_F).

As a first approximation, the CCC can be modeled like an adder element [4]. The CCC takes the advantage of the magnetic shielding properties of superconductors. Using

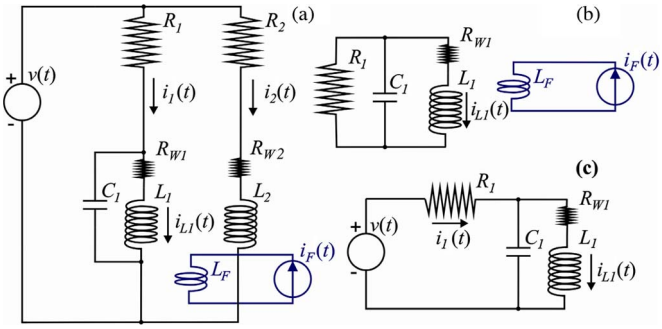

Fig. 2. (a) Simplified electrical model of the two-terminal CCC. To study this circuit, we applied the superposition principle; (b) and (c) sources are turning on one at a time.

Ampere's law, the relationship between the winding currents and the screening current (i_{screen}) in the superconductor shield is obtained [10]

$$i_{\text{screen}}(t) = i_1(t) \cdot N_1 - i_2(t) \cdot N_2 - i_F(t) \cdot N_F. \quad (1)$$

At high frequencies, the effective currents in the coils are different from the currents at the resistors due to the stray capacitances [11]. The coils have their own parasitic capacitance and a coupled parasitic capacitance with its neighbors; each coil-capacitance combination has an associated resonant frequency. To study this problem, we propose the following simplified electrical model; see Fig. 2. We take only three windings: the primary, the secondary, and the feedback winding. The first two windings are resistive, whereas the last one is superconducting. A more complex model can be used, but this would increase the complexity of the controller.

Some assumptions were considered.

1) The primary winding has the maximum value of turns and the largest stray capacitance (C_1) in the CCC.
2) The control bandwidth is limited by the self-resonant frequency of the winding with the maximum number of turns.
3) Based on the previous points, the effect of the stray capacitances of the windings, except for the primary, can be neglected.
4) The superconducting shield reduces the effective inductance of the windings due to the image effect [12].
5) The SQUID detector is considered with the flux lock loop on. The inputs to the model are small in order to maintain this feedback locked, e.g., no output voltage saturation of SQUID.
6) The simplified electrical model is considered to be linear and with concentrated parameters. With this hypothesis, the superposition principle can be applied.

In this simplified model, the primary coil is replaced by a capacitor (C_1), a resistor (R_{W1}), and an inductor (L_1), whereas the secondary winding is replaced with a resistor (R_{W2}) and an inductor (L_2), due to assumption 3). Since the feedback winding is superconducting, it is represented with an ideal inductor (L_F). The current $i_{L1}(t)$ in the ideal inductor L_1 will depend on the primary resistor current and secondary current, and feedback current. Applying the superposition principle, $i_{L1}(t)$ can be calculated as the sum of the currents in L_1 produced by $i_{1(t)}$, $i_2(t)$, and $i_F(t)$, one at a time.

The current flowing through the secondary and feedback windings will induce a current in the primary coil. This behavior can be modeled with a transfer function, and it can be calculated applying Faraday's law and solving the electrical circuit. First, we calculate the transfer function from the feedback current [Fig. 2(b)]. The mutual inductance between the primary and feedback windings is represented by M_{1F}. The voltages $v_{C1}(t)$ and $v_{L1}(t)$ are the ones across C_1 and L_1, respectively

$$v_{L1}(t) = L_1 \cdot \frac{di_{L1}(t)}{dt} - M_{1F} \cdot \frac{di_F(t)}{dt} \quad (2)$$

$$i_{L1}(t) + C_1 \cdot \frac{dv_{C1}(t)}{dt} + \frac{v_{C1}(t)}{R_1} = 0 \quad (3)$$

$$v_{C1}(t) = i_{L1}(t) \cdot R_{W1} + v_{L1}(t). \quad (4)$$

To solve the set of linear equations, we use the Laplace transform, where "s" is a complex variable represented by $s = j\omega$ (Fourier transform), with ω as the frequency. We include a subscript in the primary inductance current to indicate that it is produced by the feedback current. To distinguish between model representations, Laplace transform variables are written in uppercase, and the time variables are written in lowercase

$$I_{L1F}(s) = T_{L1F}(s) \cdot I_F(s) \quad (5)$$

$$T_{L1F}(s) = \frac{M_{1F}s \cdot (C_1 s + 1/R_1)}{C_1 L_1 s^2 + s \cdot (L_1/R_1 + C_1 R_{W1}) + (R_{W1}/R_1 + 1)}. \quad (6)$$

$T_{L1F}(s)$ is the transfer function from the feedback current to the current in the primary winding. We can calculate the transfer function from the secondary winding $(T_{L12}(s))$ in the same way, where the mutual inductances and the respective subscript have to be replaced. Also, the current flowing in L_1 as a function of $I_1(s)$, as in Fig. 2(c), can be calculated. Again, a subscript in the primary inductance current was included to indicate that it is produced by the current through the primary resistor. The resultant transfer function is called $T_{L11}(s)$

$$I_{L11}(s) = T_{L11}(s) \cdot I_1(s) \quad (7)$$

$$T_{L11}(s) = \frac{1}{C_1 L_1 s^2 + s \cdot C_1 R_{W1} + 1}. \quad (8)$$

Comparing (6) and (8), for large R_1, the denominators become identical. Now, we write the Laplace transform of (1) and replace the primary current by the effective winding current

$$I_{\text{screen}}(s) = I_{L1}(s) \cdot N_1 - I_2(s) \cdot N_2 - I_F(s) \cdot N_F. \quad (9)$$

Next, the effective current in the primary winding is replaced by (5) and (7). For simplicity, the complex variable is omitted in the following equations:

$$I_{\text{screen}} = \overbrace{(I_{L11} + I_{L1F} + I_{L12}) \cdot N_1}^{\Phi_I(s)} - I_2 N_2 - I_F N_F \quad (10)$$

$$I_{\text{screen}} = \overbrace{I_1 \cdot T_{L11} \cdot N_1 - I_2 \cdot (N_2 - T_{L12} \cdot N_1)}^{\Phi_F(s)} - \overbrace{I_F \cdot (N_F - T_{L1F} \cdot N_1)}. \quad (11)$$

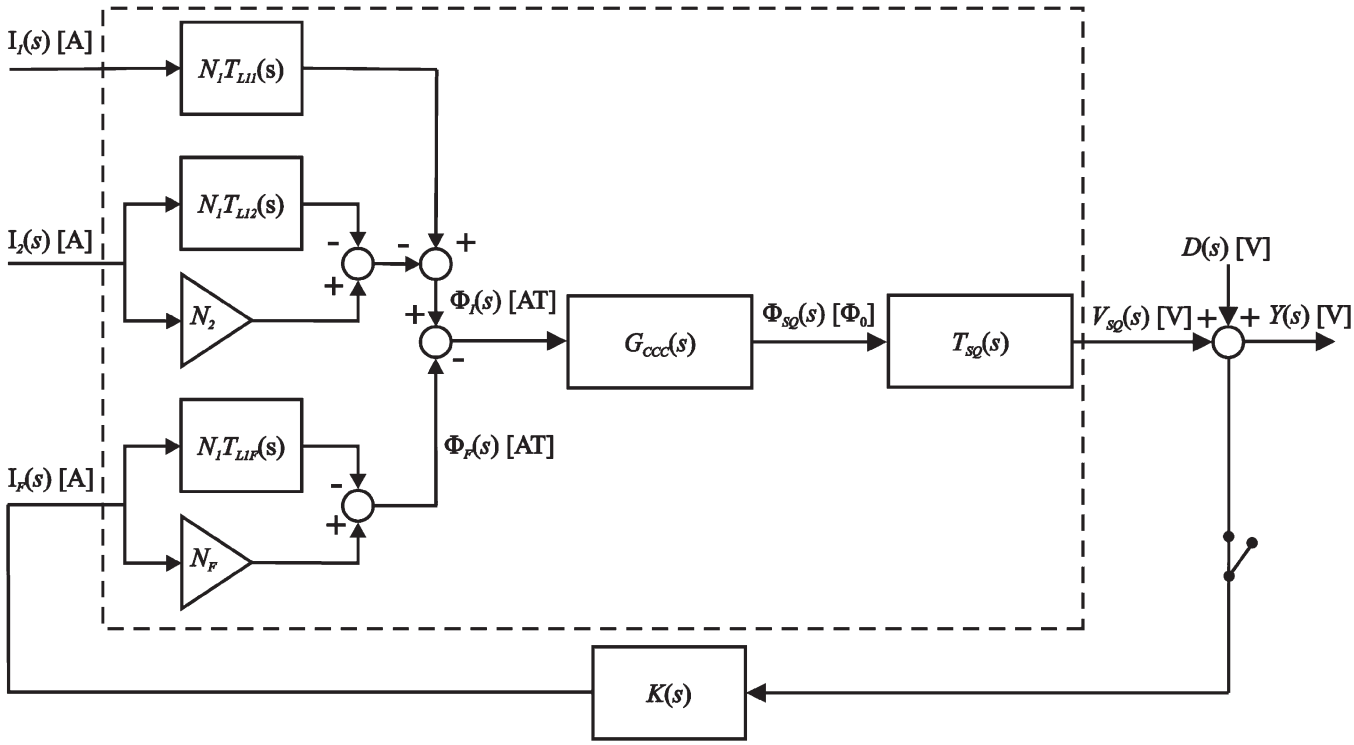

Fig. 3. Complete block diagram of the two-terminal CCC; it is equivalent to (13). The controller box $K(s)$ represents the original integral $(K_i(s))$ or the $H\infty$ controller $(K_H(s))$. In the feedback loop, a switch is included to indicate where the loop is opened.

Variable $\Phi_F(s)$ represents the total feedback flux, and $\Phi_I(s)$ represents the flux generated by the primary and secondary currents, both in ampere–turn (AT) units. The screening current is sensed with a dc SQUID. The relationship $(G_{\mathrm{CCC}}(s))$ between i_{screen} and the input flux in the SQUID $(\Phi_{SQ}(s))$ can be calculated like the inverse of the current linkage

$$\Phi_{SQ}(s) = G_{\mathrm{CCC}}(s) \cdot [\Phi_I(s) - \Phi_F(s)]. \tag{12}$$

Finally, the SQUID—from the flux input to the output voltage $(V_{SQ}(s))$—is simulated like a low-pass filter $T_{SQ}(s)$, by assumption 5)

$$V_{SQ}(s) = T_{SQ}(s) \cdot G_{\mathrm{CCC}}(s) \cdot [\Phi_I(s) - \Phi_F(s)]. \tag{13}$$

III. Set of Models

A block diagram of the whole system is shown in Fig. 3. Input "$D(s)$" is a voltage perturbation that is connected to the output of SQUID. It represents the Johnson noise, mechanic vibrations, external noise, or SQUID noise. Variable "$\Phi_I(s)$" is the reference input, and it depends on the resistor's values, the applied voltage, and the dynamics of each arm of the two-terminal CCC. These dynamics are outside the feedback loop and cannot be controlled. For this reason, we are not interested in a precise determination of $T_{L11}(s)$ and $T_{L12}(s)$ transfer functions. Only for simulation purposes, they can be calculated at ambient temperature. A different situation holds for transfer function $T_{L1F}(s)$ because it is inside the feedback loop. This function is affected by the resistor under test and by the image effect of the superconducting shield. In addition, by assumption 3), the stray capacitance of all other coils, except for the primary, was neglected. This could be unrealistic, i.e., feedback induces a current in each winding, which will decrease the total feedback flux. Robust control approaches this problem by representing the physical system behavior with a set of models, instead of a nominal one, and designing a controller that will provide stability and performance to this whole set [7], [8]. Performance is defined here as the rejection in output $Y(s)$ of a set of exogenous disturbances $D(s)$, i.e., bounded norm of $Y(s)$ for all disturbances $D(s)$ in the set $\|d(t)\|_2^2 = \int_\infty^\infty |d(t)|^2 dt < 1$. Here, the norm of $Y(s)$ is also measured as the energy integral, and $d(t)$ is the signal that corresponds to the Laplace transform $D(s)$. It is a more conservative solution, but it guarantees (robust) stability of the entire model set and, hence, of the actual system contained in it. To define the model set, first rewrite (13), where input "$\Phi_I(s)$" has been eliminated

$$V_{SQ}(s) = -\overbrace{T_{SQ}(s) \cdot G_{\mathrm{CCC}}(s) \cdot (N_F - T_{L1F}(s) \cdot N_1)}^{G} \cdot I_F(s). \tag{14}$$

The set of models used to synthesize the controller can be described as a set (Ψ) of transfer functions $G(s)$ centered in the nominal model $G_0(s)$, which is the negative of the transfer function of SQUID times the CCC gain (Fig. 4). Note that N_F is equal to one

$$\Psi = \{G(s) : G(s) = G_0(s) \cdot (1 + W_\Delta(s) \cdot \Delta), |\Delta| < 1\}. \tag{15}$$

To this end, all possible transfer functions $N_1 T_{L1F}(s)$ in (14) for the envelope of possible parameters are covered by

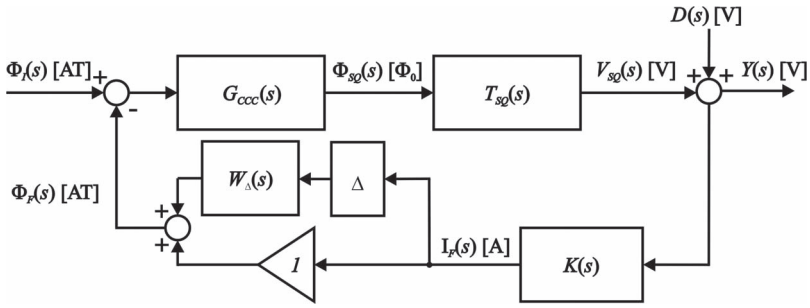

Fig. 4. Simplified block diagram of the set of models used to synthesize the controller. CCC-based amplifier and four-terminal CCC can be represented with this diagram with small modification.

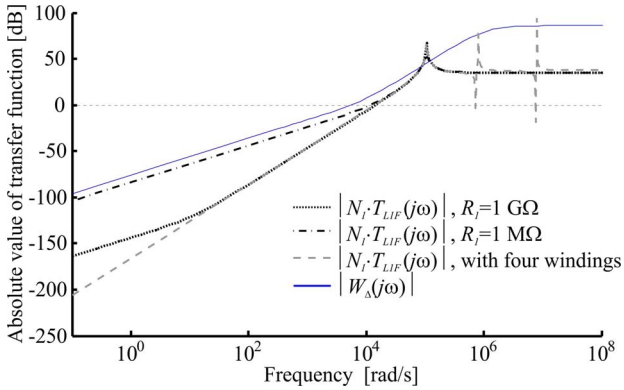

Fig. 5. Dash–dot and dotted lines are the simulations of function $N_1 \cdot T_{L1F}(s)$ for different values of the primary resistor. The dashed gray line shows a situation with four windings. The proposed weight is in solid blue line.

a weight $W_\Delta(s)$ that represents the frequency distribution of model uncertainty times the bounded uncertainty Δ, with $|\Delta| < 1$. This structure is called multiplicative dynamic uncertainty in the robust control jargon and quantifies the set of models that covers the physical system. In robust control, model uncertainty is the (frequency-dependent) radius around the nominal model and represents a deterministic quantification of the lack of knowledge of the nominal model with respect to the physical system. This should not be confused with uncertainty in the metrological sense.

The uncertainty weight is obtained by simulating the transfer function $N_1 T_{L1F}(s)$ in extreme situations, as illustrated in Fig. 5. The two-terminal CCC under study has been specially designed to measure high-value resistor (HRCCC), and it has five ratio windings: one of 3100 turns, another of 310, two of 31, and one of four turns. The first four windings have been made with resistive wire of phosphor bronze. For simulation purposes, we considered the primary winding with 3100 turns, the secondary with 310 turns, and the superconducting feedback winding of one turn. The first two windings have nominal resistances of $R_{W1} = 2800\ \Omega$ and $R_{W2} = 280\ \Omega$, respectively. The current linkage was measured during the system setup, i.e., 3.9 μAT/Φ_0. The cutoff frequency of SQUID was obtained from its specification—50 kHz [13]—and the dc gain was measured. This value is usually called flux sensitivity, and in our case, it is 0.72 V/Φ_0. The inductance of the primary winding was selected equal to the theoretical value of 1.14 H, and the capacitance value C_1 was chosen in such a way that the resultant resonant frequency agrees with that obtained in the measurement of the spectrum. Proportional values were used in other windings. The mutual inductance between the feedback or secondary coil and the primary was calculated with the worst case coupling factor of one.

First, the value of the primary resistor can attenuate the resonant peak and increase the low frequency gain of the function $N_1 T_{L1F}(s)$. This is shown in Fig. 5; the dotted line is the function $N_1 \cdot T_{L1F}(s)$ with R_1 equal to 1 GΩ and the dash–dot line with R_1 equal to 1 MΩ. In addition, the effect of other winding resonances can be simulated; the fluxes produced by the induced currents in each winding will have the same direction. The dashed gray line shows this situation with four ratio windings; the resistance connected to each winding was the estimated isolation resistance, i.e., 10 TΩ. Also, the behavior of $N_1 \cdot T_{L1F}(s)$ with other parameters, e.g., inductance, was studied, but no significant changes were obtained. Finally, the solid blue line represents the proposed uncertainty weight. To improve the closed-loop performance, the proposed weight does not completely cover all curves of the transfer function $N_1 \cdot T_{L1F}(s)$ above 0 dB. This is possible because 0 dB represents 100% relative model uncertainty, and at that value, from a control point of view, it is irrelevant if the design uncertainty represented by $W_\Delta(s)$ is larger or not, while it remains above 0 dB. In some sense, weight $W_\Delta(s)$ is used as a tuning parameter: A better performance will be obtained at frequencies where its absolute value is lower.

Fig. 6 shows the calculated transfer function from the primary and feedback currents to the voltage of SQUID. This simulation and the following were performed with the same primary inductance and resonant frequency that, before, R_1 equal to 1 GΩ and R_2 equal to 100 MΩ. Clearly, both transfer functions are dominated by the lower resonant frequency corresponding to the larger inductance. This result is coherent with the literature [4] and with experimental observations. The transfer function from the feedback current amplified above 100 dB signals below 10 MHz, and the dc gain is proportional to the winding number. Hence, this huge gain is the key feature of the CCC, although it also amplifies undesirable signals that can decrease the SQUID performance. For this reason, the main objective in the CCC design is the attenuation of any type of noise. Fig. 7 shows the response of the open-loop system to a current step of amplitude 1 μA in the feedback winding.

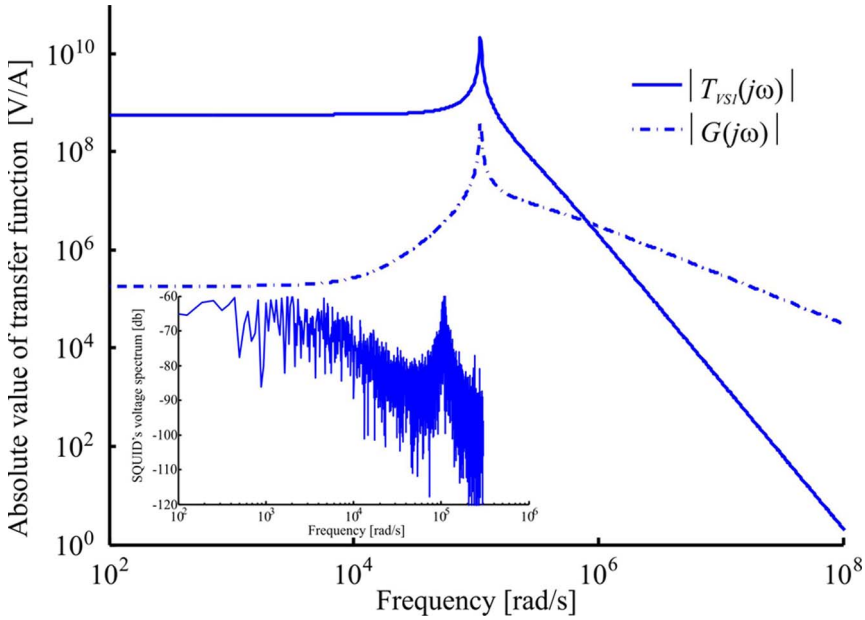

Fig. 6. Calculated transfer function of the open-loop system from the primary current $(T_{VS1}(s))$ and from the feedback current $(G(s))$ to $V_{SQ}(s)$. The voltage spectrum of SQUID, without feedback, is shown in the inset.

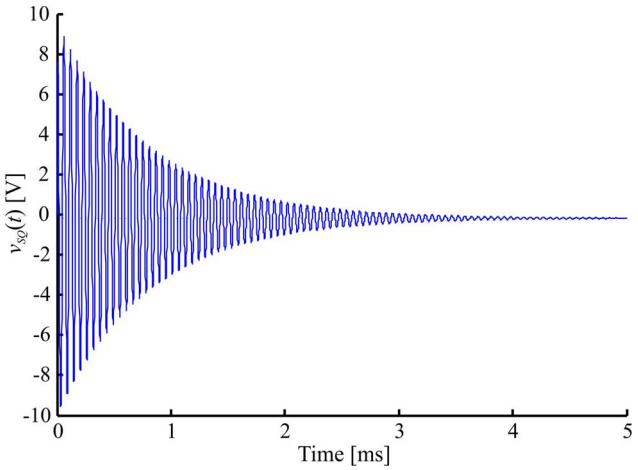

Fig. 7. Step response of the open-loop system. The primary RLC circuit produces high-frequency oscillations that can decrease the SQUID performance.

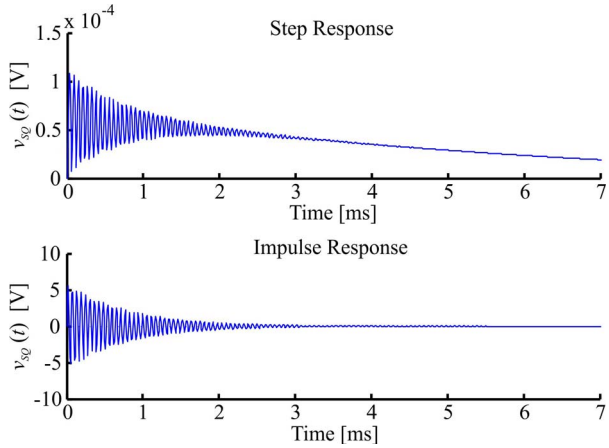

Fig. 8. Response to an impulse and step current of 0.1 pA in the primary resistor with integral control. The system amplifies more than $5 \cdot 10^{13}$ times a spike in the voltage source.

IV. Closed-Loop Behavior With Integral Control

In the HRCCC, the original controller is a low-pass filter followed by an integrator and a Howland current source. We calculate the controller's transfer function from the circuit scheme. The low-pass filter has a cutoff frequency of 122 Hz, the Howland source has a fixed gain of $1 \cdot 10^{-4}\ \Omega^{-1}$, and the calculated transfer function $(K_I(s))$ has to be multiplied by the number of turns of the feedback coil (in this case, only one turn)

$$K_I(s) = \frac{0.67}{s \cdot (s + 766.67)}. \tag{16}$$

The following figures show the step, impulse, and frequency responses of the transfer function from the primary current input to the "$Y(s)$" output. Clearly, the integral control attenuates low frequencies, and this produces that the SQUID output voltage tends to zero for the step response, as shown in Fig. 8. On the other hand, the CCC is working as a bandpass filter with a huge gain of 200 dB near the resonant frequency (see Fig. 9). This produces that high-frequency components at the input are amplified. For example, a spike in the voltage source can produce a flux jump or saturation of the SQUID controller, and this can be studied with the impulse response, as illustrated in Fig. 8.

V. Closed-Loop Behavior With $H\infty$ Control

Based on the previous sections, we find a main problem in the HRCCC: The wide bandwidth of the CCC and the slow integral feedback produce a huge amplification of the resonant frequency. In the literature, we can find only one work where this problem was considered [5]. There, a high-frequency loop in the SQUID was established to decrease the effect of

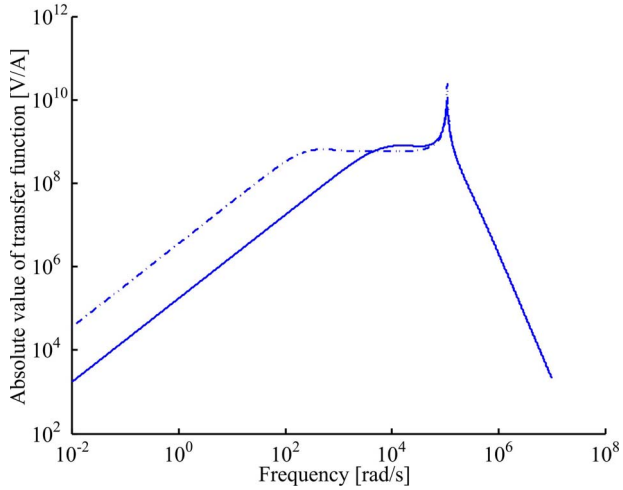

Fig. 9. Frequency response of the transfer function from the primary current input to the output of SQUID with (dash–dot line) integral control and (solid line) $H\infty$ control. The system with integral control amplified more than 100 dB signals between 0.1 Hz and 100 kHz. In addition, the resonant frequency is amplified by 200 dB. The new controller has better attenuation of undesirable signals from dc to 1.3 kHz.

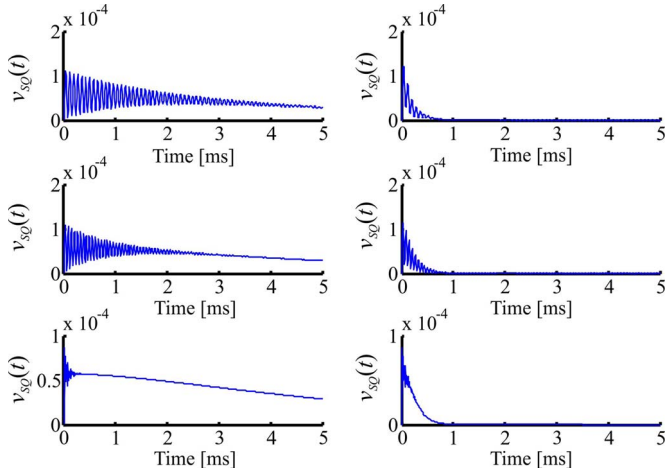

Fig. 10. Response to a step current of 0.1 pA in the primary resistor with (left) integral control and (right) $H\infty$ control. These simulations were made with the same parameters than before, but the inductances of the primary coil were (from top to bottom) 2, 1.14, and 0.1 H. With the new controller, the settling time drastically decreases, but the amplitude increases by 10%.

high-frequency noise, and the SQUID sensor was specially designed for that purpose.

Here, we propose an $H\infty$ controller that closes the loop in the traditional feedback winding. This optimal method has been used successfully for more than 20 years, and a numerically robust toolbox is available to design controllers. In this case, it adequately fits the statement of the problem and improves over previous techniques by considering sets of models and disturbances. A tradeoff design was achieved in order to find an optimal controller that maintains the closed-loop system

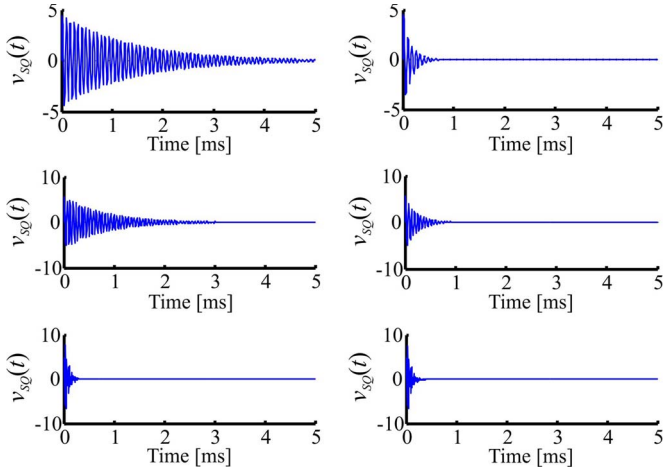

Fig. 11. Response to an impulse current of 0.1 pA in the primary resistor with (left) integral control and (right) $H\infty$ control. These simulations were made with the same parameters in Fig. 6, but the inductances of the primary coil were (from top to bottom) 2, 1.14, and 0.1 H. With the new controller, the settling time drastically decreases, and the amplitude remains constant.

(robustly) stable despite uncertainty in some parameters for a class of inputs, while increasing disturbance rejection. This controller was designed based on a mixed-sensitivity structure using the γ-iteration algorithm [7], [8]. Equation (17), shown at the bottom of the page, shows the transfer function of the $H\infty$ controller $K_H(s)$, which, at low frequencies, has an integral action.

Fig. 9 shows the frequency response of the closed-loop system. Compared with the integral control, the new controller decreases the effect of high-frequency noise more than 20 times and the resonant peak by a factor of three. It also has better step and impulse responses, as can be seen in Figs. 10 and 11. These simulations show that the $H\infty$ control reduces the effect of undesirable signals in the CCC inputs. For example, for power line frequencies (50 or 60 Hz), the new controller attenuates 21 dB more than the traditional integral control.

The transfer function from perturbation $D(s)$ to output $Y(s)$ is compared in the integral and $H\infty$ controller cases in Fig. 12. Here, again, the new controller attenuates the perturbation 20 times more, and therefore, the effect of the noise generated or coupled to the CCC or SQUID will be much lower.

VI. Conclusion and Future Research

The simulations have shown that the robust control can be successfully applied to a two-terminal CCC. Measurement systems with better noise rejection can be designed, and this can impact in lower standard deviations and systematic errors. Simulations have shown that the noise in the voltage source or in the SQUID is attenuated 26 dB more than that in the original (integral) controller. The two-terminal CCC is quite

$$K_H(s) = \frac{1.19 \cdot (s + 1.26 \cdot 10^6) \cdot (s + 1.00 \cdot 10^6) \cdot (s + 3.14 \cdot 10^5)}{(s + 5.80 \cdot 10^{10}) \cdot (s + 1.00 \cdot 10^{-6}) \cdot (s^2 + 4.18 \cdot 10^4 \cdot s + 4.52 \cdot 10^8)} \tag{17}$$

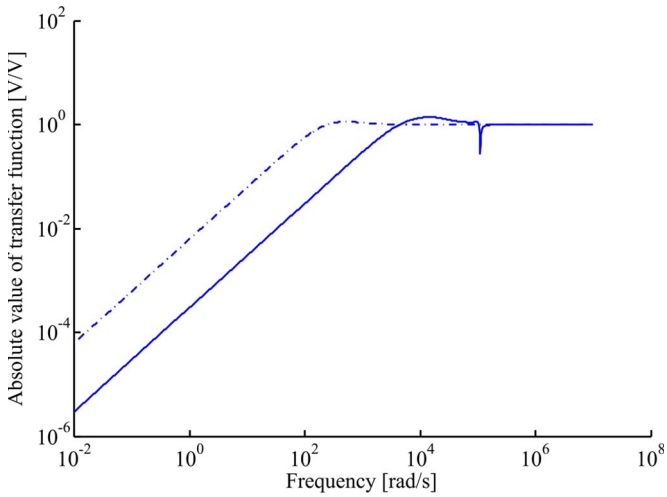

Fig. 12. Transfer function in log scale from the perturbation $D(s)$ to the output $Y(s)$ with (solid line) the $H\infty$ controller and (dash–dot line) the integral controller.

similar to a CCC-based current amplifier [14]. In this way, the results presented in this paper can be applied, with small modifications, to single electron tunneling measurements and quantum metrological triangle. In addition, this work can be extended to a four-terminal CCC.

The resulting $H\infty$ controller has to be implemented with digital technology, and a higher frequency bandwidth will result in the feedback loop. To calculate the resistor's ratio, the feedback current has to be measured at dc. High-frequency components could affect this measurement; therefore, extra filtering could be necessary. To avoid this, two feedback loops could be used: one for low and the other for high frequencies (see also [5]).

In this paper, we have assumed a complete lack of knowledge in the model above 1.5 kHz. If a model identification process of the physical system is performed, the uncertainty weight could be decreased, and as a consequence, the closed-loop performance could be increased even more.

REFERENCES

[1] M. E. Bierzychudek and A. Tonina, "High resistance measurement with a two-terminal cryogenic current comparator," in *Proc. CPEM Dig.*, Washington, DC, USA, 2012, pp. 372–373.

[2] P. Kleinschmidt, J. M. Williams, N. E. Fletcher, and T. J. B. M. Janssen, "Cryogenic current comparator bridge for quantum Hall resistance ratio measurements," *Proc. Inst. Elect. Eng.—Sci. Meas. Technol.*, vol. 149, no. 6, pp. 302–304, Nov. 2002.

[3] C. A. Sanchez, B. M. Wood, and A. D. Inglis, "CCC bridge with digitally controlled current source," *IEEE Trans. Instrum. Meas.*, vol. 58, no. 4, pp. 1202–1205, Apr. 2009.

[4] K. Jones and M. D. Early, "A quantum hall cryogenic current comparator resistance bridge," in *Proc. CPEM Dig.*, Sydney, NSW, Australia, 2000, pp. 92–93.

[5] M. Götz, D. Drung, E. Pesel, H. J. Barthelmess, C. Hinnrichs, C. Aßmann, M. Peters, H. Scherer, B. Schumacher, and T. Schurig, "Improved cryogenic current comparator setup with digital current sources," *IEEE Trans. Instrum. Meas.*, vol. 58, no. 4, pp. 1176–1182, Apr. 2009.

[6] R. E. Elmquist, E. Hourdakis, D. G. Jarrett, and N. M. Zimmerman, "Direct resistance comparisons from the QHR to 100 MΩ using a cryogenic current comparator," *IEEE Trans. Instrum. Meas.*, vol. 54, no. 2, pp. 525–528, Apr. 2005.

[7] R. S. Sánchez Peña and M. Sznaier, *Robust Systems: Theory and Applications*. Hoboken, NJ, USA: Wiley, 1998.

[8] K. Zhou, J. Doyle, and K. Glover, *Robust and Optimal Control*. Englewood Cliffs, NJ, USA: Prentice-Hall, 1996.

[9] M. Bierzychudek and R. E. Elmquist, "Uncertainty evaluation in a two-terminal cryogenic current comparator," *IEEE Trans. Instrum. Meas.*, vol. 58, no. 4, pp. 1170–1175, Apr. 2009.

[10] J. M. Williams, "Cryogenic current comparators and their application to electrical metrology," *IET Sci. Meas. Technol.*, vol. 5, no. 6, pp. 211–224, Nov. 2011.

[11] K. Grohmann and D. Hechtfischer, "Self-calibrating cryo current comparators for AC applications," *IEEE Trans. Instrum. Meas.*, vol. IM-33, no. 2, pp. 91–96, Jun. 1984.

[12] J. Sesé, F. Lera, A. Camón, and C. Rillo, "Calculation of effective inductances of superconducting devices. Application to the cryogenic current comparator," *IEEE Trans. Appl. Supercond.*, vol. 9, no. 1, pp. 58–62, Mar. 1999.

[13] DC + RF SQUID Systems Brochure, Quantum Design. [Online]. Available: http://www.qdusa.com/sitedocs/productBrochures/squid3.pdf

[14] F. Piquemal and G. Geneves, "Argument for the direct realization of the quantum metrological triangle," *Metrologia*, vol. 37, no. 3, pp. 207–211, 2000.

M. E. Bierzychudek received the Electronic Engineering degree from the Universidad de Buenos Aires, Buenos Aires, Argentina, in 2006.

In 2005, he joined the Electricity Division, Instituto Nacional de Tecnología Industrial, San Martín, Argentina, where he has worked since then in the Voltage and Resistance Laboratory and is involved in measurements of the Josehpson effect and the quantum Hall effect.

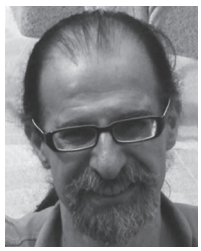

R. S. Sánchez–Peña (SM'00) received the Electronic Engineering degree from the University of Buenos Aires, Buenos Aires, Argentina, in 1978 and the M.S. and Ph.D. degrees from California Institute of Technology, Pasadena, CA, USA, in 1986 and 1988, respectively.

From 1977 to 2004, he worked in several research institutions in Argentina. He was also a Professor with the University of Buenos Aires (1989–2004), an Institució Catalana de Recerca i Estudis Avançats Research Professor with the Universitat Politécnica de Catalunya, Barcelona, Spain (2004–2009), and a Visiting Researcher and a Professor at universities in the U.S. and Europe. He worked in aerospace projects with the National Aeronautics and Space Administration, German Aerospace Centre, Departamento de Ciência e Tecnologia Aeroespacial/Instituto Nacional de Pesquisas Espaciáis (Brazil), and ZonaTech (AZ, USA). Since 2009, he has directed the Ph.D. Program at the Buenos Aires Institute of Technology (ITBA), Buenos Aires, as a Consejo Nacional de Investigaciones Científícas y Técnicas Principal Investigator. He published three books and more than 120 journal and conference papers. His research interests include the applications of robust identification and control to practical problems in engineering and medicine.

Dr. Sánchez–Peña is a full member of the International Academy of Astronautics and a senior member of the American Institute of Aeronautics and Astronautics, and he was a Policy Committee member of the International Federation of Automatic Control (2005–2008).

Alejandra Tonina was born in Buenos Aires, Argentina, in 1962. She received the Licenciatura and Ph.D. degrees in physics from the University of Buenos Aires, Buenos Aires, in 1993 and 1998, respectively.

Since 1998, she has been with the Instituto Nacional de Tecnología Industrial, San Martín, Argentina, where she is currently in charge of the Quantum Electrical Metrology Laboratory.